A New Control Architecture With Spatial Comb Filter and Spatial Repetitive Controller for Circulating Current Harmonics Elimination in a Droop-Regulated Modular Multilevel Converter for Wind Farm Application

Sandeep Kolluri, *Student Member, IEEE*, Naga Brahmendra Yadav Gorla, *Student Member, IEEE*, Rajesh Sapkota, and Sanjib Kumar Panda, *Senior Member, IEEE*

***Abstract*—Circulating current control is one of the critical issues in modular multilevel converters (MMCs). When a frequency-droop-regulated MMC is used to integrate an offshore wind farm into an high-voltage dc transmission system, the variation in its operating ac line frequency induces a change in circulating current harmonic frequencies. Hence, the conventional circulating current controllers, such as proportional-resonant or repetitive controller, which are tuned to a specific frequency, fail to alleviate the circulating current harmonics. In this paper, a new control architecture comprising of a spatial comb filter (SCF) and a spatial repetitive controller (SRC) is proposed to effectively attenuate the even-order harmonics in the circulating current independent of the operating ac line frequency of the MMC. The proposed controller incorporates the phase sampling technique to achieve the dynamic change in the sampling frequency, which is the key to strong periodic disturbance rejection capability of the SCF and SRC even under variable frequency operation. A system level simulation model has been developed on PLECS simulation software to demonstrate the performance of the proposed control architecture. In addition, a scaled-down laboratory prototype of a 1-kW, 400-V, five-level single-phase MMC is developed and the experimental results are presented to substantiate the performance of the proposed control scheme.**

***Index Terms*—Adaptive comb filter, circulating current harmonics, frequency adaptive periodic control, frequency droop control, HVdc transmission, modular multilevel converter, offshore wind farm integration, spatial comb filter (SCF), spatial repetitive controller (SRC).**

I. Introduction

In HIGH and medium-voltage applications, a modular multilevel converter (MMC) has emerged as a promising alternative to the traditional multilevel power converter

Manuscript received August 27, 2018; revised December 21, 2018; accepted January 26, 2019. Date of publication February 4, 2019; date of current version August 29, 2019. Recommended for publication by Associate Editor L.Chang. *(Corresponding author: Sanjib Kumar Panda.)*

The authors are with the Electrical and Computer Engineering Department, National University of Singapore, Singapore 117580 (e-mail:

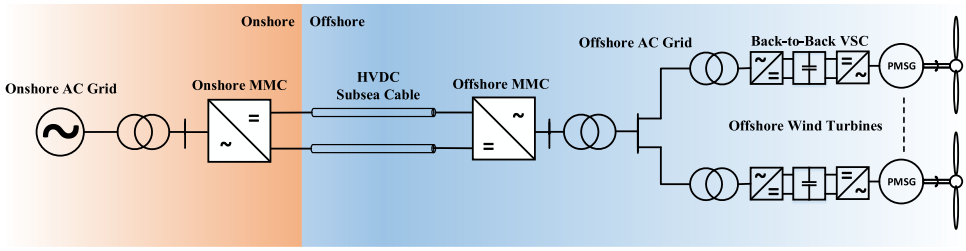

Fig. 1. Block diagram of an MMC-based HVdc transmission system for the offshore wind farm integration.

the offshore ac grid. All the back-to-back voltage source converters (VSCs) in the individual wind turbines are connected to the offshore ac grid. In general, frequency droop control is employed in large wind farms to vary the active power set points of each wind turbine, which is equipped with a full power back-to-back VSC [19]. Droop control facilitates the decentralized control, thereby, eliminating the requirement for intercommunication between the offshore MMC and the wind turbines. The centralized control is expensive, as it requires high bandwidth communication infrastructure and is less reliable as well. Whereas, in the decentralized control, the active power flow from each turbine is enabled by local measurements available to the back-to-back VSC, which makes it less expensive and more reliable. In order to control the flow of the active power from individual wind turbines, the offshore MMC alters the line frequency, which in turn alters the flow of the active power from the back-to-back VSCs according to their designed droop characteristics. This scenario can lead to a substantial change in the operating ac line frequency of the offshore MMC, which in turn varies the harmonic frequencies in the circulating current. Hence, the traditional circulating current controller based on a PR controller, which is tuned to a specific harmonic frequency, or a time-domain repetitive controller with fixed sampling frequency will not be able to suppress the even-order harmonics in the circulating current occurring at varying frequencies.

In [20] and [21], a double frequency negative sequence rotating reference-frame-based circulating current suppressing controller has been proposed. In such reference frame, the second harmonic of the circulating current would appear as a dc component, therefore, a conventional PI controller can be used to effectively attenuate the second harmonic in the circulating current independent of the operating line frequency of the MMC, as the controller is synchronized with the line frequency using a phase-locked loop (PLL). However, to attenuate multiple even-order harmonics in the circulating current, multiple of such reference frames should be defined, which increases the control complexity. Moreover, the implementation of such controllers in an unbalanced three-phase system poses challenge.

In [22], authors have proposed a circulating current suppressing strategy based on non-ideal PR controller, in which gain of the proposed controller is spread around the tuned frequency, unlike in an ideal PR controller. Therefore, this controller can damp out the harmonics even with a deviation in the operating line frequency of the MMC. But this method would be effective only for a very limited range of frequency variation, due to its gain characteristics and the proposed controller offers a reduced gain at the tuned frequency compared to its ideal counterpart.

To overcome the aforementioned issues, a new circulating current control structure comprising of a spatial comb filter (SCF) and a spatial repetitive controller (SRC) is proposed in this paper, to effectively attenuate the even-order harmonics in the circulating current in a frequency-droop-regulated MMC used for the wind farm integration into the HVdc transmission system. The proposed control architecture reduces the current stress on the switching devices and improves the operating efficiency of the MMC.

Phase sampling technique, which helps in achieving dynamic change in the sampling frequency, is a key to the implementation of both SCF and SRC. As the SCF and SRC are implemented based on the line-voltage phase angle sample position ($\theta = \int \omega_o dt$) [23]–[25], ω_o being the fundamental frequency, the gain characteristics of the SCF and SRC are independent of the operating ac line frequency of the MMC, and therefore, can effectively attenuate the circulating current harmonics even under variable frequency operation of the MMC.

An SCF can adaptively adjust its attenuation characteristics according to the operating line frequency of the MMC, such that the dominant second-order harmonic component of the submodule capacitor voltage ripple is filtered out even under variable frequency operation of the MMC. Besides, the frequency adaptive nature and high gain of the SRC at even-order harmonic frequencies make it effective in rejecting the periodic disturbances even at variable frequencies. Its gain characteristic gets tuned according to the operating line frequency of the MMC and effectively eliminates the even-order circulating current harmonics even under variable frequency operation of the MMC, thus improving its operating efficiency.

This paper is organized as follows: A simplified mathematical analysis is carried out in this paper to delve into reason for the presence of the dominant second harmonic in both the circulating current and submodule capacitor voltages, and this is presented in Section II. Drawbacks of the existing circulating current control schemes for the MMC are discussed in Section III. Analysis and design of the proposed circulating current control architecture is presented in Section IV. A system level simulation model has been developed on PLECS simulation software to demonstrate the performance of the proposed control architecture and the simulation results are presented in Section V. A scaled-down laboratory prototype of a 1-kW, 400-V, five-level single-phase MMC has been developed and the experimental results are presented in Section VI, to substantiate the performance of the proposed SCF- and SRC-based circulating current controller. Conclusions are presented in Section VII.

II. Mathematical Modeling of the MMC

The circuit configuration of a three-phase MMC with half-bridge submodules is shown Fig. 2. Each phase leg comprises

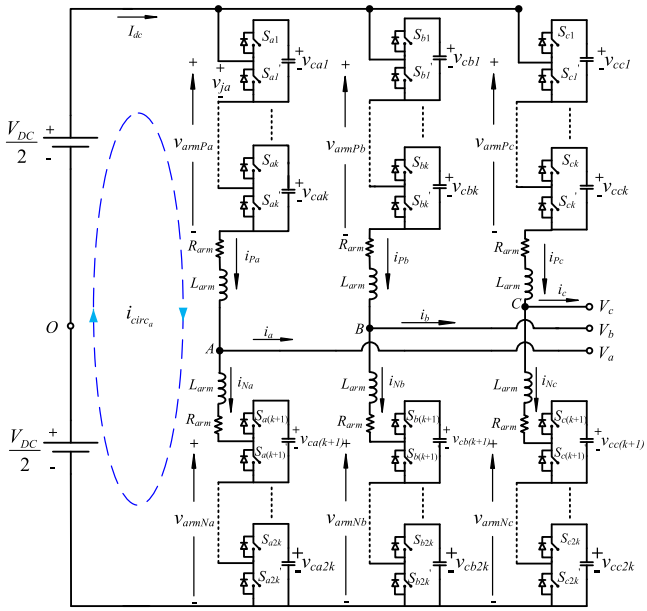

Fig. 2. Circuit configuration of the three-phase MMC.

of an upper arm and a lower arms. Whereas, each arm consists of k series-connected identical half-bridge submodules and an inductor L_{arm}. Upper arm and lower arm in each phase leg are represented by the subscripts P and N, respectively. In the literature, various types of submodule topologies have been proposed, out of which the most conventional submodule topologies are the full bridge and half bridge [2]. In this paper, a half-bridge submodule is considered for the analysis.

A. General Circuit Analysis

Arm currents in an MMC are continuous unlike in the traditional power converter topologies. The ac output current of phase a, i_a, is split between the upper and lower arms, each carrying half of it. The upper and lower arm currents are given by (1) and (2), respectively. The current distribution must be guaranteed by the control strategy.

$$i_{P_a} = i_{\text{circ}_a} + \frac{i_a}{2} \tag{1}$$

$$i_{N_a} = i_{\text{circ}_a} - \frac{i_a}{2} \tag{2}$$

where i_{P_a}, i_{N_a}, and i_{circ_a} are the currents in the upper arm, lower arm, and circulating current in phase a, respectively.

By adding (1) and (2), the output ac currents are cancelled out, the circulating current obtained is

$$i_{\text{circ}_a} = \frac{i_{P_a} + i_{N_a}}{2}. \tag{3}$$

From Fig. 2, by applying Kirchhoff's voltage law to the upper and lower sides of each phase leg, the output per phase voltage equations are obtained and are given by (4) and (5).

$$v_{ao} = \frac{V_{\text{dc}}}{2} - v_{\text{arm}Pa} - L_{\text{arm}}\frac{di_{P_a}}{dt} - R_{\text{arm}} i_{P_a} \tag{4}$$

$$v_{ao} = -\frac{V_{\text{dc}}}{2} + v_{\text{arm}Na} + L_{\text{arm}}\frac{di_{N_a}}{dt} + R_{\text{arm}} i_{N_a} \tag{5}$$

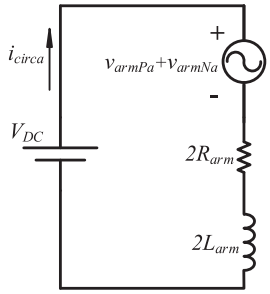

Fig. 3. Per phase equivalent circuit for the circulating current in the three-phase MMC.

where $v_{\text{arm}Pa} = \sum_{j=1}^{k} v_{ja}$ and $v_{\text{arm}Na} = \sum_{j=k+1}^{2k} v_{ja}$. v_{ja} is the jth submodule terminal voltage in phase a. By subtracting (4) from (5), substituting the arm current and circulating current equations given by (1)–(3), the following expression can be obtained:

$$V_{\text{dc}} = (v_{\text{arm}Pa} + v_{\text{arm}Na}) + 2L_{\text{arm}}\frac{di_{\text{circ}_a}}{dt} + 2R_{\text{arm}} i_{\text{circ}_a}. \tag{6}$$

The per phase equivalent circuit for the circulating current in a three-phase MMC [17] derived from (6) is shown in Fig. 3. The circulating current is a unique feature of the MMC, which consists of a dc component and an unwanted ac component as given in (7). The dc component of the circulating current, $i_{\bar{\text{circ}}_a}$, is responsible for the transfer of the power to the submodules in each leg.

$$i_{\text{circ}_a} = i_{\bar{\text{circ}}_a} + i_{\tilde{\text{circ}}_a}. \tag{7}$$

The ac component of the circulating current, $i_{\tilde{\text{circ}}_a}$, is generated due to the voltage differences naturally produced due to the voltage ripple in submodule capacitors. It has been reported that this component comprises of a dominant second-order harmonic and other higher even-order harmonics [16]. The circulating currents of the phase a in the MMC is given by

$$i_{\text{circ}_a} = \frac{I_{\text{dc}}}{3} + \sum_{n=1}^{\infty} I_{2nf} \sin(2n\omega_o t + \phi_{2nf}) \tag{8}$$

where I_{dc} is the magnitude of dc bus current, I_{2nf} is the magnitude of even-order harmonic current, ω_o is the fundamental frequency of the ac output current i_a, and $n = 1, 2, 3....$ The ac component of the circulating current brings additional loss and current stress to the system, thus, it is not desirable. The primary cause for the generation of even-order harmonics in the circulating current is analyzed in the following sub-section.

B. Circulating Current Harmonic Analysis

To simplify the mathematical equations while delving into the primary cause for the presence of dominant second harmonic in both the circulating current and the submodule capacitor voltages, we can assume an equal and a constant dc voltage across every submodule capacitor. In this case, the ideal circulating current component in each phase would be dc and equal to $\frac{I_{\text{dc}}}{3}$. Therefore, the upper and lower arm currents of phase a are given

by (9) and (10), respectively.

$$i_{P_a} = \frac{I_{\text{dc}}}{3} + \frac{I_a}{2}\sin(\omega_o t - \theta) \tag{9}$$

$$i_{N_a} = \frac{I_{\text{dc}}}{3} - \frac{I_a}{2}\sin(\omega_o t - \theta). \tag{10}$$

Modulation signals for the upper arm and lower arm of phase a are defined by (11) and (12), respectively.

$$m_{P_a} = M_{P_a}\sin(\omega_o t) \tag{11}$$

$$m_{N_a} = M_{N_a}\sin(\omega_o t) \tag{12}$$

where M_{P_a} and M_{N_a} are the modulation indices. The corresponding average switching functions for the upper arm and lower arm are given by (13) and (14), respectively.

$$S_{P_a} = \left(\frac{1 - M_{P_a}\sin(\omega_o t)}{2}\right) \tag{13}$$

$$S_{N_a} = \left(\frac{1 + M_{N_a}\sin(\omega_o t)}{2}\right). \tag{14}$$

Using (9)–(14), the submodule capacitor currents of the upper and lower arm can be written as (15) and (16), respectively.

$$i_{CP_a} = \left(\frac{I_{\text{dc}}}{3} + \frac{I_a}{2}\sin(\omega_o t - \theta)\right)\cdot\left(\frac{1 - M_{P_a}\sin(\omega_o t)}{2}\right) \tag{15}$$

$$i_{CN_a} = \left(\frac{I_{\text{dc}}}{3} - \frac{I_a}{2}\sin(\omega_o t - \theta)\right)\cdot\left(\frac{1 + M_{N_a}\sin(\omega_o t)}{2}\right). \tag{16}$$

Equations (17) and (18) can be derived by expanding and segregating similar frequency terms in (15) and (16). One can observe that the submodule capacitor currents i_{CP_a} and i_{CN_a} consists of three components: dc component, fundamental component, and second harmonic component. The reason for generation of the second harmonic component is multiplication of two sinusoidal terms: $\frac{I_a}{2}\sin(\omega_o t - \theta)$ and $\frac{M_{P_a}}{2}\sin(\omega_o t)$, which are at fundamental frequency. Equations (17–21) as shown at the bottom of the next page.

For the MMC to be operated in a stable state, the dc component of the submodule capacitor currents given in (17) and (18) should be equal to zero. This means while the dc bus current, i_{dc}, charges the submodule capacitor, the ac output current, i_a, discharges it.

$$v_{CP_a} = \bar{V}_{\text{dc}} + \tilde{v_{CP_a}} \tag{22}$$

$$v_{CN_a} = \bar{V}_{\text{dc}} + \tilde{v_{CN_a}}. \tag{23}$$

Now, we can find the voltage ripple component on the submodule capacitors using (17) and (18). v_{CP_a} and v_{CN_a} given by (22) and (23), represents the sum of the submodule capacitor voltages in the upper arm and the lower arm, respectively, where $v_{CP_a} = \sum_{j=1}^{k} v_{ca_j}$ and $v_{CN_a} = \sum_{j=k+1}^{2k} v_{ca_j}$, v_{ca_j} is jth submodule capacitor voltage in phase a. At steady state, v_{CP_a} and v_{CN_a} consists of two components: a dc component, which is equal to dc bus voltage V_{dc}, and a ripple component. The ripple components $\tilde{v_{CP_a}}$ and $\tilde{v_{CN_a}}$ can be derived by integrating the ac component of i_{CP_a} and i_{CN_a} and are given by (19) and (20), respectively. From (19) and (20), we can observe that the submodule capacitors have a voltage ripple at both fundamental (ω_o) and second harmonic frequency ($2\omega_o$).

$$v_{\text{csum}_a} = v_{CP_a} + v_{CN_a} = 2\bar{V}_{\text{dc}} + \tilde{v_{CP_a}} + \tilde{v_{CN_a}} \tag{24}$$

$$\tilde{v_{\text{csum}_a}} = \tilde{v_{CP_a}} + \tilde{v_{CN_a}} = \underbrace{\frac{kI_a M_{P_a}}{8\omega_o c}\sin(2\omega_o t - \theta)}_{2^{\text{nd}}\text{harm. component}}. \tag{25}$$

The voltage, v_{csum_a}, is defined as sum of upper arm and lower arm submodule capacitor voltages in phase a and is given by (24). To find the ripple component of v_{csum_a}, which is defined as $\tilde{v_{\text{csum}_a}}$, (19) and (20) should be added and is given by (25), assuming *MPa* and *MNa* are equal. When the ripple component on the upper arm and lower arm submodule capacitor voltages is summed up, fundamental frequency component of the voltage ripple gets cancelled out and the second-order harmonic component gets doubled, which can be observed from (25). The second harmonic voltage ripple, $\tilde{v_{\text{csum}_a}}$, has a detrimental effect on the performance of the circulating current controller, which is explained in the following section and it should be effectively filtered out while using v_{csum_a} as a feedback control variable. As

$$i_{CP_a} = \underbrace{\frac{I_{\text{dc}}}{6} - \frac{I_a M_{P_a}}{8}\cos(\theta)}_{\text{DC component}} + \underbrace{\frac{I_a}{4}\sin(\omega_o t - \theta) - \frac{I_{\text{dc}} M_{P_a}}{6}\sin(\omega_o t)}_{\text{fundamental component}} + \underbrace{\frac{I_a M_{P_a}}{8}\cos(2\omega_o t - \theta)}_{\text{2nd harm. component}} \tag{17}$$

$$i_{CN_a} = \underbrace{\frac{I_{\text{dc}}}{6} - \frac{I_a M_{N_a}}{8}\cos(\theta)}_{\text{DC component}} - \underbrace{\frac{I_a}{4}\sin(\omega_o t - \theta) + \frac{I_{\text{dc}} M_{N_a}}{6}\sin(\omega_o t)}_{\text{fundamental component}} + \underbrace{\frac{I_a M_{N_a}}{8}\cos(2\omega_o t - \theta)}_{\text{2nd harm. component}} \tag{18}$$

$$\tilde{v_{CP_a}} = \frac{k}{c}\int \tilde{i_{CP_a}}\,dt = \underbrace{-\frac{kI_a}{4\omega_o c}\cos(\omega_o t - \theta) + \frac{kI_{\text{dc}} M_{P_a}}{6\omega_o c}\cos(\omega_o t)}_{\text{fundamental component}} + \underbrace{\frac{kI_a M_{P_a}}{16\omega_o c}\sin(2\omega_o t - \theta)}_{\text{2nd harm. component}} \tag{19}$$

$$\tilde{v_{CN_a}} = \frac{k}{c}\int \tilde{i_{CN_a}}\,dt = \underbrace{\frac{kI_a}{4\omega_o c}\cos(\omega_o t - \theta) - \frac{kI_{\text{dc}} M_{N_a}}{6\omega_o c}\cos(\omega_o t)}_{\text{fundamental component}} + \underbrace{\frac{kI_a M_{N_a}}{16\omega_o c}\sin(2\omega_o t - \theta)}_{\text{2nd harm. component}} \tag{20}$$

$$v_{\text{arm}Pa} + v_{\text{arm}Na} = \underbrace{V_{\text{dc}} + \frac{kI_a M_{P_a}}{8\omega_o c}\sin(\theta)}_{\text{DC component}} + \underbrace{\frac{kM_{P_a}}{4\omega_o c}\left(\frac{I_a}{4} - \frac{I_{\text{dc}} M_{P_a}}{3}\right)\sin(2\omega_o t)}_{\text{2nd harm. component}} + \underbrace{\frac{kI_a M_{P_a}}{8\omega_o c}\sin(2\omega_o t - \theta)}_{\text{2nd harm. component}} \tag{21}$$

the arm voltages, v_{armPa} and v_{armNa} are generated by modulating the submodule capacitor voltage v_{CP_a} and v_{CN_a}, respectively, the propagation of the submodule capacitor voltage ripple into the arm voltage can be found by using (26) and (27).

$$v_{\text{armPa}} = v_{CP_a} \cdot \left(\frac{1 - M_{P_a} \sin(\omega_o t)}{2} \right) \tag{26}$$

$$v_{\text{armNa}} = v_{CN_a} \cdot \left(\frac{1 + M_{N_a} \sin(\omega_o t)}{2} \right). \tag{27}$$

Summing up the upper arm voltage v_{armPa} and the lower arm voltage v_{armNa} results in (21), which has a dc component and second harmonic components.

From (6), defining v_{limb} as the voltage across the arm inductor, we can write

$$\begin{aligned} 2L_{\text{arm}} \frac{di_{\text{circ}_a}}{dt} + 2R_{arm} i_{\text{circ}_a} &= V_{\text{dc}} - (v_{\text{armPa}} + v_{\text{armNa}}) \\ &= v_{\text{limb}}. \end{aligned} \tag{28}$$

Some conclusions can be drawn by analyzing (21) and (28). The circulating current i_{circ_a} depends on the dc bus voltage and the sum of the upper and lower submodules terminal voltages in one leg. Ideally, the sum of upper arm and lower arm voltages should be a dc voltage, but due to the propagation of the second harmonic voltage ripple of the submodule capacitor into the arm voltage, a second harmonic component can be observed in (21). This results in second harmonic voltage drop across the arm inductor, which drives the second harmonic component in the circulating current. Further, this second harmonic current flows through the arm, causing higher order voltage harmonics on submodule capacitors and this in turn results in higher order harmonics in the circulating current, leading to a cascaded effect.

The internal circulating current control loop of the MMC modifies the modulation commands m_{P_a} and m_{N_a}, which are generated by the external line voltage control loop. The output of the circulating current controller is subtracted from the modulation commands of the upper arm and lower arm, before they are fed to the modulator. Hence, the circulating current controller generates an additional control voltage v_c across the arm inductor. Hence, from (6) and (28), we can derive the following:

$$\begin{aligned} 2L_{\text{arm}} \frac{di_{\text{circ}_a}}{dt} + 2R_{\text{arm}} i_{\text{circ}_a} &= V_{\text{dc}} - (v_{\text{armPa}} + v_{\text{armNa}}) + v_c \\ &= v_{\text{limb}} + v_c. \end{aligned} \tag{29}$$

However, if the operating line frequency of the MMC, ω_0, varies, the frequency at which the harmonics occur in the submodule capacitor voltage and circulating current also varies accordingly. Therefore, the main aim of this paper is to design a filter that can effectively dampen out the harmonics in v_{csum_a}, which is a feedback variable, and a circulating current controller that generates v_c to counteract the periodic disturbance in the arm voltage, in order to alleviate harmonics in the circulating current even under variable frequency operation of the MMC.

III. Existing Circulating Current Control Schemes

The conventional cascaded structure for the circulating current control in the MMC [26] based on the PI controller, shown in Fig. 4, consists of total energy control loop as the outer loop, which controls sum of all submodule capacitor voltages v_{csum} in a phase leg to follow the reference command. The output of

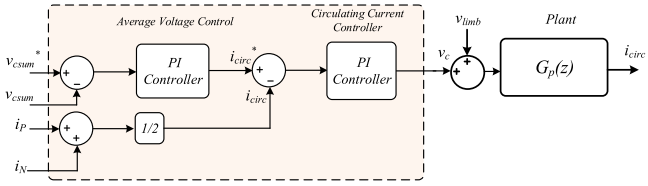

Fig. 4. Existing control architecture of the circulating current control with a PI controller.

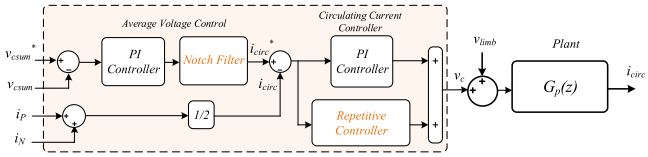

Fig. 5. Existing control architecture of the circulating current control with a notch filter and a repetitive controller.

the outer total energy control loop is fed as a circulating current reference for the inner circulating current control loop. The flow of energy from the dc link to the submodule capacitors is controlled by the inner circulating current control loop. However, the gains of the PI controller in the outer total energy control loop are restricted due to the dominant second harmonic voltage ripple component of v_{csum}. This is to prevent the propagation of the low-frequency harmonic component of v_{csum} into the circulating current reference. But this might lead to sluggish dynamic response of the circulating current controller, especially during the load transients. This means during a load transient, the transition of the circulating current reference becomes slower due to restricted bandwidth of the outer total energy control loop. This introduces a considerable amount of deviation in submodule capacitor voltages as a result of mismatch in the instantaneous input and output power during the transient. Further, depending on the nature of the load transient, the deviation in the submodule capacitor voltages reflects as a voltage sag or swell in the ac output voltage of the MMC.

On the other hand, the inner circulating current control loop should track the current reference generated by the outer total energy control loop. In addition, it should also suppress the even-order harmonic components in the circulating current caused due to the even-order harmonic components in the arm voltages. However, the PI controller has high gain at dc or zero frequency, but not at harmonic frequencies. Therefore, a PI controller is only suitable for the step disturbance rejection but not for the periodic disturbances.

In order to restrict the propagation of low-frequency harmonic components into the circulating current reference one can use the notch filter in the outer total energy control loop, as shown in Fig. 5, which is tuned to the second-order harmonic frequency. This allows design of the PI controller in the outer loop with required bandwidth without any restrictions. Whereas in the inner loop a time-domain-based repetitive controller with fixed sampling frequency, shown in Fig. 5, which is based on the internal model principle can be incorporated in parallel with the PI controller to deal with periodic disturbances in the arm voltages [27]. Its ability to reject the disturbances at multiple harmonic frequencies makes it appropriate for the elimination of even-order harmonics in the circulating current. The repetitive

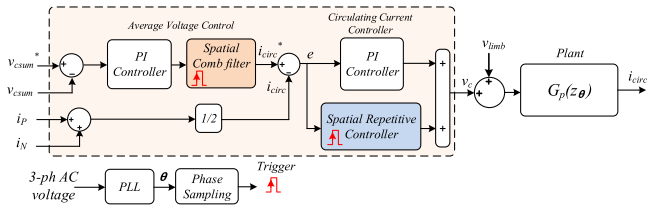

Fig. 6. Proposed control architecture of the circulating current control with an SCF and an SRC.

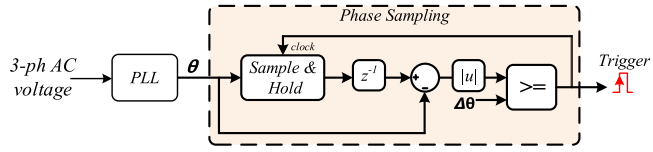

Fig. 7. Implementation of the phase sampling circuit.

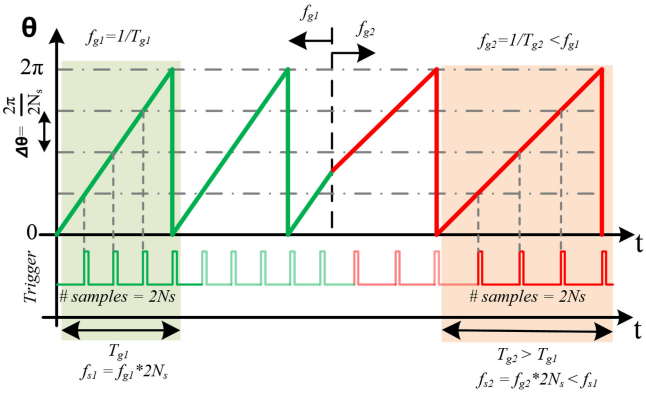

Fig. 8. Phase sampling technique to achieve a dynamic change in the sampling frequency and to maintain fixed number of samples per cycle $2N_s$ irrespective of the fundamental ac line frequency f_g of the offshore MMC.

controller integrates the error and takes action on a cycle by cycle basis. The transfer function of the repetitive controller [16] can be written as

$$G_{\rm rc}(z) = Q(z)K_{\rm rc}\frac{z^{-(N-N_1)}}{1-z^{-N}} \tag{30}$$

where $K_{\rm rc}$ is the positive gain of the repetitive controller, $Q(z)$ is a low pass filter, N is the number of samples per cycle, and $N_1(N_1 < N)$ is the number of advancement samples given to compensate the phase delay of the plant.

However, as discussed in the earlier section, due to droop control, the operating frequency of the offshore MMC might vary. Therefore, the notch filter and the repetitive controller, which are tuned to the rated frequency, fail to attenuate even-order harmonics in the circulating current reference and circulating current.

IV. Proposed Circulating Current Control Scheme

For effective operation of the repetitive controller, the frequency of the second-order harmonic component in the circulating current should be an integral fraction of sampling frequency, i.e., $\frac{f_s}{2f_g} = N_s$, where N_s is a large integer, f_s is the sampling frequency, and f_g is fundamental ac line frequency. But, if the frequency of the second-order harmonic component varies, the time-domain-based repetitive controller with fixed sampling frequency becomes ineffective in alleviating the harmonics. Hence, the sampling frequency must be varied according to the frequency of the second-order harmonic component, such that the number of samples N_s is constant. However, varying the sampling frequency in accordance with the frequency of the second-order harmonic component in the circulating current is a challenging task. At steady state, the discrete complex frequency at the fundamental ac line frequency, f_g, can be given as $z = e^{j\omega_o T_s}$, where $\omega_o = 2\pi f_g$ and sampling time $T_s = \frac{1}{f_s}$. If the number of samples per cycle can be maintained constant according to the relation $\frac{f_s}{2f_g} = N_s$, then at steady state, z can be given as $z = z_\theta = e^{j\frac{2\pi}{2N_s}} = e^{j\Delta\theta}$. This explains that the dynamic change in the sampling frequency can be achieved by sampling the system at multiples of the fundamental space phase $\Delta\theta = \frac{2\pi}{2N_s}$. Therefore, the proposed control architecture shown in Fig. 6, with the SCF in the outer total energy control loop and the SRC in the inner circulating current loop, samples the system at multiples of fundamental space phase $\Delta\theta$ and takes control action at those corresponding discrete samples of fundamental phase $\theta = n\frac{2\pi}{2N_s}$, where $n = 1, 2, 3....2N_s$.

A. Phase Sampling Circuit

A phase sampling circuit is incorporated in the proposed control architecture, which samples the phase angle information of the ac line voltage, generated by a PLL. Implementation of the phase sampling circuit, which is one of the critical element in the proposed controller, is shown in Fig. 7. The phase sampling circuit consists of a sample and hold block, which samples the phase angle (θ) when its clock input goes high. The clock input to the sample and hold block is generated by a comparator block, whose output toggles when the difference between sampled phase angle and the actual phase angle is greater than or equal to $\Delta\theta$. The phase sampling technique to achieve the dynamic change in the sampling frequency is illustrated in Fig. 8. As the phase angle always varies from 0 to 2π, irrespective of the fundamental ac line frequency, by fixing the value of $\Delta\theta$, one can generate fixed number of samples per cycle even with the variation in the line frequency. From Fig. 8, we can observe number of samples per cycle remain constant, even though the fundamental ac line frequency f_g is varied from f_{g1} to f_{g2}. Output of the comparator block shown in Fig. 7, serves as a trigger signal for the proposed SCF and SRC. Hence, the SCF and SRC can adaptively tune their gain characteristics to mitigate the propagation of even-order harmonic components in the circulating current reference and the circulating current, respectively, without being affected by the variation in the fundamental ac line frequency [28].

B. Plant Transfer Function in Phase Sample Domain

From Fig. 3 and (28), we can define the continuous plant transfer function for the circulating current model as

$$G_p(s) = \frac{i_{\rm circ}(s)}{v_{\rm limb}(s)} = \frac{1}{2L_{\rm arm}} \cdot \frac{1}{s + \frac{R_{\rm arm}}{L_{\rm arm}}}. \tag{31}$$

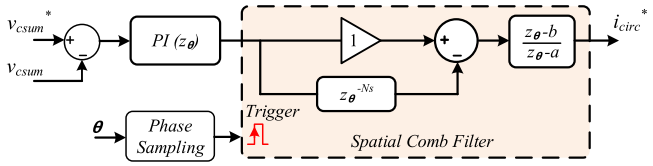

Fig. 9. Block diagram of the proposed SCF.

By discretizing the aforementioned transfer function using a forward Euler method, the discrete plant transfer function $G_p(z)$ for the circulating current model can be derived as

$$G_p(z) = \frac{i_{\text{circ}}(z)}{v_{\text{limb}}(z)} = \frac{T_s}{2L_{\text{arm}}} \cdot \frac{1}{z - (1 - \frac{R_{\text{arm}}}{L_{\text{arm}}} T_s)} \tag{32}$$

where T_s is the sampling period. However, the proposed control scheme takes control action at multiples of fundamental space phase $\Delta\theta$, but not at sampling period T_s. By using the equations $T_s = \frac{1}{f_s}$, $N_s = \frac{f_s}{2f_g}$, $\Delta\theta = \frac{2\pi}{2N_s}$ and $\omega_o = 2\pi f_g$, we can derive that $T_s = \frac{\Delta\theta}{\omega_o}$. Therefore, by replacing T_s in (32) with $\frac{\Delta\theta}{\omega_o}$, the discrete plant transfer function $G_p(z_\theta)$ for the circulating current model in the phase sample domain is given by

$$G_p(z_\theta) = \frac{i_{\text{circ}}(z_\theta)}{v_{\text{limb}}(z_\theta)} = \frac{\Delta\theta}{2\omega_o L_{\text{arm}}} \cdot \frac{1}{z_\theta - \left(1 - \frac{R_{\text{arm}}}{\omega_o L_{\text{arm}}} \Delta\theta\right)}. \tag{33}$$

C. Spatial Comb Filter (SCF)

An SCF in the total energy control loop, shown in Fig. 9, prevents the propagation of the even-order harmonics in v_{csum} into the circulating current reference i_{circ}^*, irrespective of the variation in the operating ac line frequency of the MMC. For this to happen, an SCF should offer high attenuation to the harmonic components of v_{csum} and also the attenuation characteristics should adapt to the change in harmonic frequencies resulted due to the variation in the ac line frequency.

The discrete transfer function for a digital comb filter in the time-domain sampling with sampling period T_s is given by

$$G_{\text{comb}}(z) = \frac{z - b}{z - a} \left(1 - z^{-N_s}\right). \tag{34}$$

Here, $(1 - z^{-N_s})$ is the filter part of the transfer function, which offers high attenuation to any harmonic component with a time period, which is equal to $N_s T_s$ or an integral fraction of $N_s T_s$. Hence, for a given sampling period T_s, by appropriately choosing the value of N_s, unwanted even-order harmonic components can be eliminated from the circulating current reference.

As discussed earlier, if the harmonic frequencies vary due to change in operating ac line frequency of the MMC, the digital comb filter fails to attenuate the even-order harmonic components in the circulating current reference. This is because of the fixed sampling period T_s. Therefore, an SCF in the phase sampling domain is proposed in this paper and the corresponding discrete transfer function is given by

$$G_{\text{scomb}}(z_\theta) = \frac{z_\theta - b}{z_\theta - a}(1 - z_\theta^{-N_s}). \tag{35}$$

In the phase sampling domain, the sampling period $T_s = \frac{\Delta\theta}{\omega_o}$, varies dynamically according to the fundamental operating ac line frequency of the MMC, ω_o. Even though N_s is fixed, due to its ability in achieving the dynamic change in the sampling period T_s according to the ac line frequency, an SCF can adjust its attenuation characteristics such that even-order harmonic components in the circulating current reference are filtered even under variable frequency operation of the MMC. However, $(1 - z_\theta^{-N_s})$ offers attenuation to the dc component of the circulating current reference as well. Since this dc component should not be attenuated, the filter part of the transfer function is multiplied with $\frac{z_\theta - b}{z_\theta - a}$, to compensate for the attenuation effect at dc as shown in Fig. 10. The variable a decides the location of pole in the z-plane and is chosen to be 1 so that the transfer function $\frac{z_\theta - b}{z_\theta - a}$ offers a high gain at dc or zero frequency. On the other hand, variable b decides the location of zero in the z-plane. It is chosen such that the gain characteristics of $\frac{z_\theta - b}{z_\theta - a}$ does not affect the attenuation characteristics of $(1 - z_\theta^{-N_s})$ at harmonic frequencies. Accordingly, b is chosen to be 0.95.

The value of $\Delta\theta$ is chosen to be $\frac{\pi}{20}$, and hence, 40 samples per fundamental ac cycle are achieved, as θ varies from 0 to 2π irrespective of the ac line frequency. By setting the value of N_s as 20, which is half the number of total samples per fundamental ac cycle, the filter offers attenuation to even-order harmonics. The same design values have been used for both simulation and experimental studies. The corresponding frequency response characteristics of the proposed SCF is shown in Fig. 11. The dotted lines in the frequency response signifies the adaptive nature of the proposed filter to changes in the grid frequency. Assuming the rated ac line frequency is 50 Hz, from Fig. 11, we

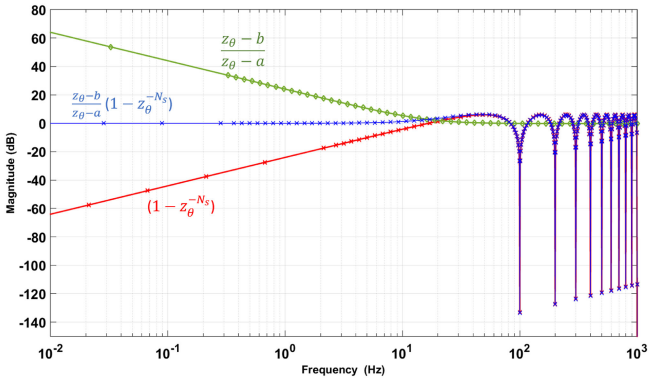

Fig. 10. Frequency response of the proposed SCF for $a = 1, b = 0.95$, $N_s = 20$, $\Delta\theta = \pi/20$, and $\omega_0 = 100\ \pi$rad/s.

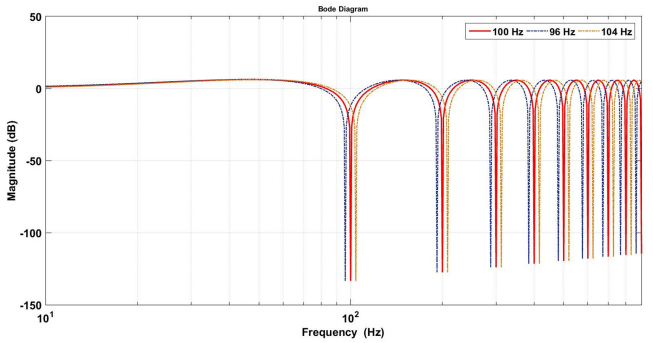

Fig. 11. Frequency response of the proposed SCF. Dotted lines signify the frequency adaptive nature of the proposed filter.

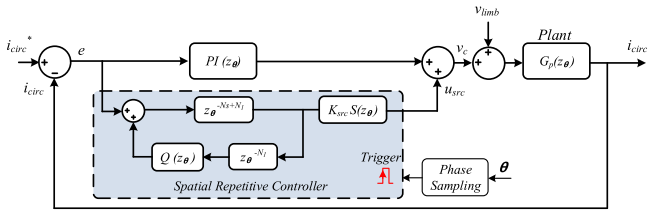

Fig. 12. Block diagram of the proposed SRC.

can observe the filter offers very high attenuation (solid line) to 100 Hz and corresponding even-order harmonics. When the line frequency of the MMC changes to 48 or 52 Hz, the attenuation characteristics (dotted lines) shift accordingly. This ensures the circulating current reference to be a near dc quantity.

D. Spatial Repetitive Controller (SRC)

Block diagram of the spatial repetitive control scheme for suppressing the circulating current is shown in Fig. 12. The transfer function of the SRC [23] is given by

$$G_{\text{src}}(z_\theta) = \frac{u_{\text{src}}(z_\theta)}{e(z_\theta)} = K_{\text{src}} S(z_\theta) \frac{z_\theta^{-(N_s - N_1)}}{1 - Q(z_\theta) z_\theta^{-N_s}} \tag{36}$$

where $u_{\text{src}}(z_\theta)$ is the control output of the SRC, $e(z_\theta)$ is the circulating current tracking error, K_{src} is the positive gain of the SRC, $N_1 (N_1 < N_s)$ is the number of advancement samples given to compensate the phase delay of the plant, $Q(z_\theta)$ is a stabilization filter, $S(z_\theta)$ is a second-order low-pass filter, which filters out the switching harmonic content in the error signal. $Q(z_\theta)$ can be a low-pass filter or a close-to-unity constant, which is often incorporated to increase the stability margin [16]. $S(z_\theta)$ is chosen as a second-order low-pass filter with a corner frequency at $\omega_n = 20\omega_o$ and the damping ratio of 1, whereas $Q(z_\theta)$ is chosen as 0.99 for simplicity and the same parameters are used for both simulation and experimental studies.

In the phase sample domain, the control law for the SRC can be written as

$$u_{\text{src}}(i, \theta_m) = u_{\text{src}}(i-1, \theta_m) + K_{\text{src}} \cdot e(i-1, \theta_{m+N_1}) \tag{37}$$

where $u_{\text{src}}(i, \theta_m)$ is the control output of the SRC at the mth position sample in the ith iteration cycle, and $e(i-1, \theta_{m+N_1})$ is the error of the reference and output at the $(m+N_1)$th position sample in the $(i-1)$th iteration cycle.

The frequency response characteristic of the SRC is shown in the Fig. 13. High gain of the controller at even-order harmonic frequencies makes it effective in rejecting the periodic disturbances at those frequencies. Due to its frequency adaptive nature, the gain characteristic gets tuned according to the operating line frequency of the MMC.

From Fig. 12, the circulating current $i_{\text{circ}}(z_\theta)$ can be derived as

$$i_{\text{circ}}(z_\theta) = \frac{(\text{PI}(z_\theta) + G_{\text{src}}(z_\theta)) G_p(z_\theta)}{1 + (\text{PI}(z_\theta) + G_{\text{src}}(z_\theta)) G_p(z_\theta)} \cdot i_{\text{circ}}^*(z_\theta) + \frac{G_p(z_\theta)}{1 + (\text{PI}(z_\theta) + G_{\text{src}}(z_\theta)) G_p(z_\theta)} \cdot v_{\text{limb}}(z_\theta). \tag{38}$$

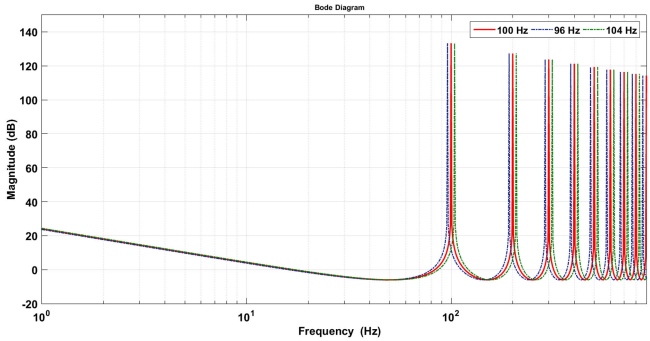

Fig. 13. Frequency response of the proposed SRC. Dotted lines signify the frequency adaptive nature of the proposed controller.

Whereas, the tracking error $e(z_\theta)$ can be derived as

$$e(z_\theta) = \frac{i_{\text{circ}}^*(z_\theta) - G_p(z_\theta) \cdot v_{\text{limb}}(z_\theta)}{1 + (\text{PI}(z_\theta) + G_{\text{src}}(z_\theta)) G_p(z_\theta)}. \tag{39}$$

The characteristic polynomial equation of the spatial repetitive control system can be given as

$$\begin{aligned} H(z_\theta) &= 1 + (\text{PI}(z_\theta) + G_{\text{src}}(z_\theta)) G_p(z_\theta) \\ &= (1 + \text{PI}(z_\theta) G_p(z_\theta)) \cdot (1 + G_{\text{src}}(z_\theta) C_{\text{cl}}(z_\theta)) \end{aligned} \tag{40}$$

where $C_{\text{cl}}(z_\theta) = \frac{G_p(z_\theta)}{1 + \text{PI}(z_\theta) G_p(z_\theta)}$ is the closed-loop transfer function from the disturbance input $v_{\text{limb}}(z_\theta)$ to the circulating current $i_{\text{circ}}(z_\theta)$, before an SRC is added to the system. From the characteristic equation given in (40), we can derive conditions for the stability of the system. The first condition is, the PI controller $\text{PI}(z_\theta)$ should be designed such that the roots of the polynomial equation $1 + \text{PI}(z_\theta) G_P(z_\theta)$ are inside the unit circle, to ensure that the system is stable before the SRC is added to the system. The second stability condition, which gives insight into the design criteria of the SRC, is that the roots of the polynomial equation $1 + G_{\text{src}}(z_\theta) C_{\text{cl}}(z_\theta) = 0$ should be strictly within the unit circle for the system to be stable after the SRC is added. By substituting (36) into $1 + G_{\text{src}}(z_\theta) C_{cl}(z_\theta) = 0$ and rearranging the terms, we can derive

$$z_\theta^{N_s} - [Q(z_\theta) - K_{\text{src}} S(z_\theta) z_\theta^{N_1} C_{\text{cl}}(z_\theta)] = 0. \tag{41}$$

Therefore, the necessary and sufficient condition for the stability of the system with the SRC is given as [16], [17], [29]

$$|Q(z_\theta) - K_{\text{src}} S(z_\theta) z_\theta^{N_1} C_{cl}(z_\theta)]| < 1. \tag{42}$$

Define, $T(e^{j\omega T_s}) = Q(e^{j\omega T_s}) - K_{\text{src}} S(e^{j\omega T_s}) e^{jN_1 \omega T_s} C_{\text{cl}}(e^{j\omega T_s})$, in the phase sampling domain $T_s = \frac{\Delta\theta}{\omega_o}$. For the stable operation of the system, magnitude of the vector $|T(e^{j\omega T_s})|$ for $\omega \in [0, \pi/T_s]$, should never exceed the unit circle.

Design Procedure: Equation (42) is crucial for the design of the SRC. First, the number of advancement samples N_1 to compensate the phase delay of the plant is chosen as one sample so that the phase delay of $S(z_\theta) C_{\text{cl}}(z_\theta)$ is effectively compensated at harmonic frequencies. Fig. 14 shows the phase response $S(z_\theta) C_{\text{cl}}(z_\theta)$ and $z_\theta^{-N_1}$, with $N_1 = 1$ and it can be observed that their phase is nearly equal at harmonic frequencies. Therefore $z_\theta^{N_1}$, with $N_1 = 1$ can cancel out the phase delay of the $S(z_\theta) C_{\text{cl}}(z_\theta)$ at harmonic frequencies. Then, using

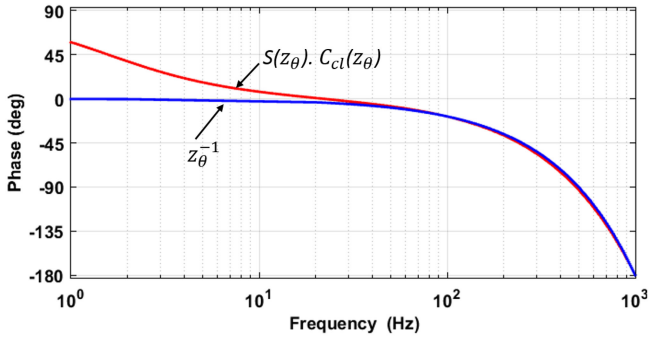

Fig. 14. Bode plot showing phase response of $S(z_\theta)C_{\text{cl}}(z_\theta)$ and $z_\theta^{-N_1}$, with $N_1 = 1$.

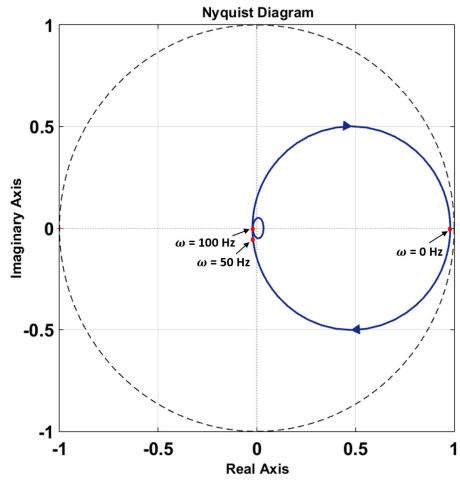

Fig. 15. Nyquist plot of $|T(e^{j\omega T_s})|$, with $T_s = \frac{\Delta\theta}{\omega_o}$, $\Delta\theta = \pi/20$, and $\omega_0 = 100\ \pi$rad/s.

the condition given in (42), gain of the SRC, K_{src} is selected for simulation and experimental studies. With $K_{\text{src}} = 0.01$ and for parameters of system analyzed in the simulation study, the Nyquist plot for $T(e^{j\omega T_s})$ is shown in Fig. 15 from which we can observe the locus of the vector is well within the unit circle ensuring the stability of the system. A similar analysis has been performed for the experimental system and a gain of 0.03 is chosen accordingly.

V. Simulation Results

In this section, system level simulation results have been presented to demonstrate the performance of the proposed circulating current controller. The schematic of the MMC-based HVdc transmission system for the offshore wind farm integration is shown in Fig. 1. A simplified simulation model [30] of the same has been developed in PLECS simulation software and is shown in Fig. 16. Assuming the dynamics in the dc-link voltage of the offshore MMC are minimal during the chosen simulation period, the dc link is modeled as a constant dc voltage source. As we are studying the effect of the proposed controller on the dominant low-frequency harmonics in the circulating current, the switching harmonics can be neglected, and therefore, an averaged model is used for the offshore three-phase MMC to keep the design simple and to increase the simulation speed. On the wind farm side, all the wind turbine generators with two-level

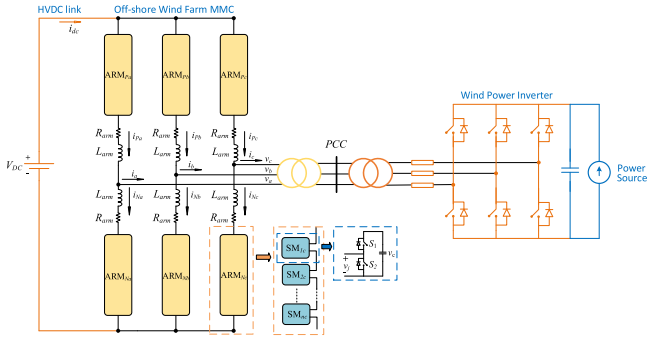

Fig. 16. Simplified configuration of a three-phase MMC integrating an offshore wind farm into the HVdc transmission system.

TABLE I
Simulation Parameters

Wind Farm MMC		Wind Power Inverter	
Rated Power	50 MW	Rated Power	50 MW
Rated Frequency	50 Hz	Rated Frequency	50 Hz
Rated DC Link Voltage	320 kV	Rated DC Link Voltage	1100 V
Rated Terminal Voltage	166 kV	Rated Terminal Voltage	690 V
No. of SMs per Arm	20	Rated Voltage at PCC	166 kV
Submodule Capacitance	100 μF	Filter Inductor	25 μH
Arm Inductance and Resistance	10 mH and 0.01 Ω		

TABLE II
Control Parameters

Controller	Parameter	Value
Spatial Repetitive Controller	K_{src}	0.01
	N_s	20
	N_1	1
Circulating Current PI controller	K_p & K_i	0.01 & 0.1
Average Voltage PI Controller	K_p & K_i	0.0005 & 0.01

back-to-back power electronic converters are modeled as an aggregated two-level wind power inverter with a power source. As the generator-side converter in the back-to-back configuration is decoupled from the grid side converter by a dc-link capacitor, the wind turbine generator and the converter can be modeled as power source. The specifications of the modeled system and the control parameters are given in Tables I and II respectively. The effect of droop control on various parameters of the offshore MMC is shown in Fig. 17. The plot shows line frequency, HVdc link power, per phase point of common coupling (PCC) voltages and PCC currents. We can observe as the line frequency is changed, the HVdc link power is varied accordingly and the corresponding variation in the PCC currents is also shown. As the main concern is to study the effect of the variable line frequency on circulating current harmonics, the performance of the existing and proposed circulating controller during these conditions is shown in Figs. 18 and 19, respectively.

Fig. 18 shows the effect of the notch filter and repetitive controller (refer to Fig. 5) on the circulating current reference generated by the total energy control loop and the actual circulating current flowing through phase A of the three-phase offshore MMC. The result has been divided into four sections, where the MMC is operating at a 50-Hz line frequency for first three sections. The first section shows the result with both

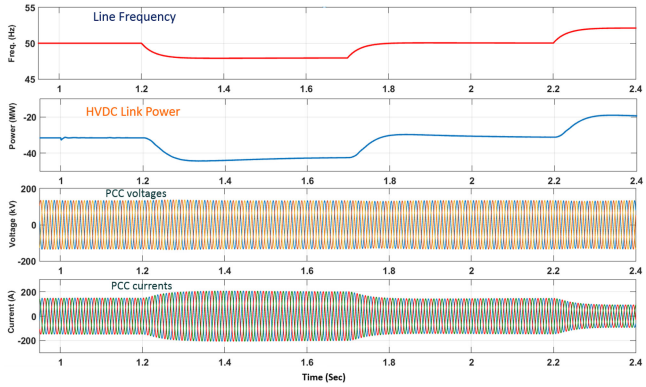

Fig. 17. Simulation results showing effect of droop control on the MMC line frequency, HVdc link power, and three-phase PCC voltages and currents.

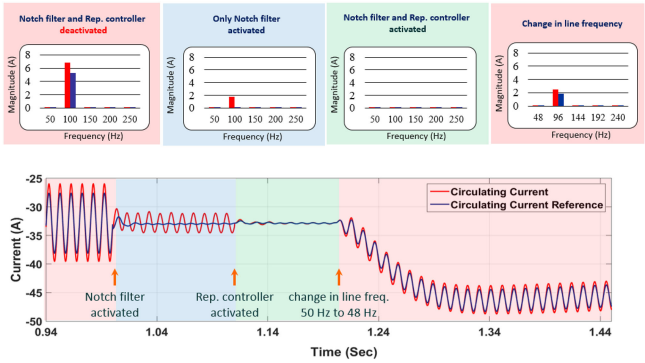

Fig. 18. Simulation results demonstrating the performance of the notch filter + repetitive-controller-based circulating current controller.

notch filter and repetitive controller being deactivated where we can observe both the reference and actual current has unwanted dominant second-order harmonic at 100 Hz in addition to the dc component. This is due to the voltage ripple component of v_{csum_α} which is fed to the outer total energy control loop. Significant gain of the outer voltage loop PI controller at 100 Hz results in second-order harmonic in the circulating current reference. We can observe the ripple component in the actual current is greater than the reference, which is due to harmonics in the arm voltage. Once the notch filter, which has been tuned to 100 Hz, is activated, the reference current becomes a near dc quantity as shown in the second section of the result. In spite of that, a significant magnitude of the second harmonic is still seen in the actual current due to inability of the inner loop PI controller to counter act the harmonic disturbance in the arm voltages. When the fixed sampling frequency plug-in repetitive controller, tuned to counter act even-order harmonic disturbance in the inner loop is activated, the dominant second-order harmonic in the circulating current gets attenuated. However, at the end of the third section, when the MMC operating line frequency changes from 50 to 48 Hz, the even-order harmonics (at 96 Hz) reappear in both reference and actual circulating current. This is because the notch filter and repetitive controller are tuned for 100 Hz and corresponding harmonic frequencies and they lack the adaptability to the external varying grid conditions. Hence, the notch filter + repetitive-controller-based circulating current control scheme fails to suppress the harmonics in the circulating current at frequencies other than the rated frequency. These harmonics can lead to device stress, submodule capacitor stress, and excessive power loss in the converter.

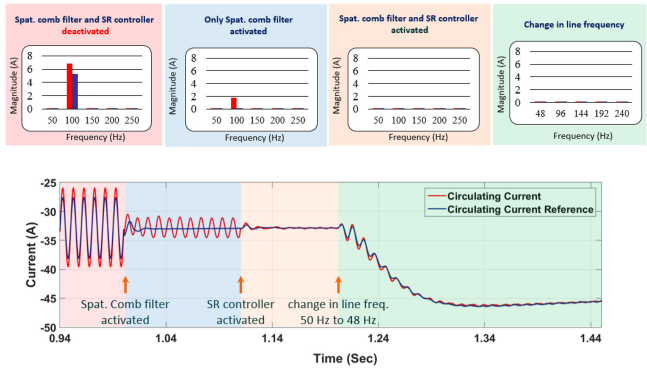

Fig. 19. Simulation results demonstrating the performance of the proposed SCF + SRC-based circulating current controller.

Fig. 19 shows the results with the proposed SCF in the outer total energy control loop and the SRC in the inner circulating current control loop. In the first section of the result, the reference and circulating current consists of the dominant second harmonic component, however, by activating SCF and SRC, the second-order harmonic is greatly attenuated, which can be observed in second and third sections of the simulation result. When the line frequency is changed from 50 to 48 Hz, the second-order harmonic component appears initially in both the reference and actual circulating current. This is due to the change of the ripple voltage frequency across sum of the submodule capacitors from 100 to 96 Hz and change of even-order harmonic frequencies in the arm voltage from 100 to 96 Hz and its multiples. Since the SCF is a frequency adaptive filter, it gets tuned soon to the new frequency and ripple components in the reference dies within a few number of cycles. Similarly, the SRC gets tuned to new frequency of periodic disturbance in the arm voltages and successfully attenuates the even-order harmonics in the circulating current. Therefore, in spite of the change in the operating line frequency of the MMC, the proposed SCF and SRC are able to attenuate harmonics in the circulating current, and hence, improves the steady-state performance of the converter by reducing the ripple current stress on submodule capacitors and power loss in the devices.

VI. Experimental Results and Discussion

The main aim of this section is to experimentally validate the performance of the proposed SCF- and SRC-based circulating current control scheme. Therefore, an experimental prototype of a 1-kW, five-level, single-phase MMC is developed and it has been demonstrated that the proposed controller is able to effectively attenuate the even-order harmonics in the circulating current of a single-phase MMC, even though the harmonic frequencies vary due to the change in the fundamental ac line frequency. Since the harmonics in the circulating current are not affected by the direction of the power flow, an *RL* load is connected on the ac side of the MMC and varied its operating line frequency. This simplifies the test bed development process without losing the test effectiveness.

The experimental prototype of the single-phase MMC comprises of an upper arm and a lower arm, whereas each arm

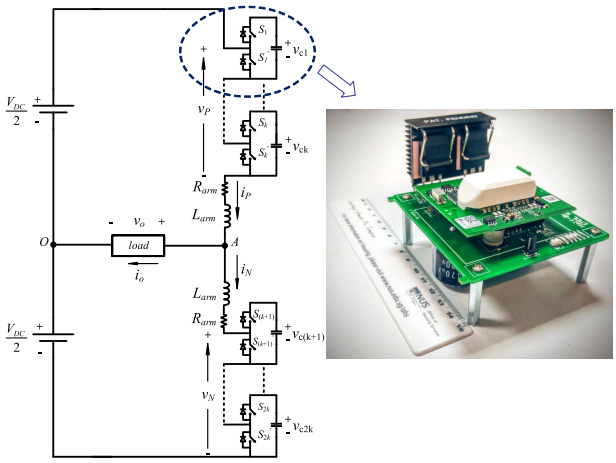

Fig. 20. Schematic diagram of the single-phase MMC and laboratory prototype of a half-bridge submodule.

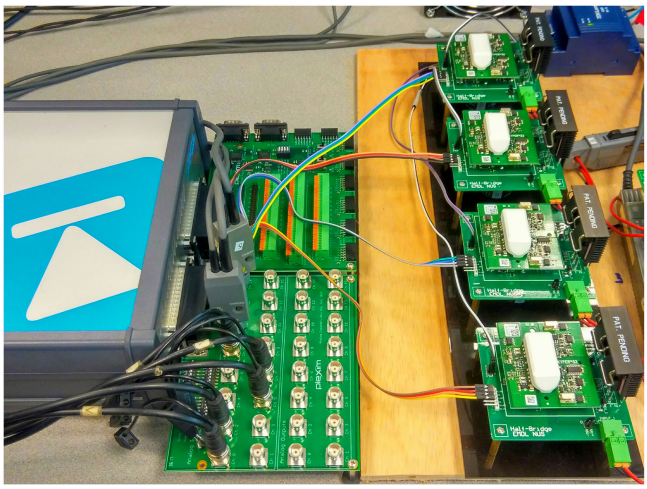

Fig. 21. Laboratory prototype of a 1-kW five-level single-phase MMC with four half-bridge submodules and a PLECS RT box for controller implementation.

consists of two half-bridge submodules. Fig. 20 shows the developed IGBT-based half-bridge submodule, which is a basic building block of the single-phase MMC. Four such half-bridge submodules are used to realize the five-level single-phase MMC as shown in Fig. 21. An arm inductance of 2.5 mH is used in each arm and a submodule capacitance of 0.96 mF is used in each half-bridge submodule . Carrier phase-shifted sinusoidal pulsewidth modulation (PWM) is employed to generate the multilevel voltage within the arms of the single-phase MMC. Each arm is modulated with two triangular carrier waves, which are 180° $(360^\circ/k)$ phase shifted, k is the number of submodules per arm. The switching frequency of the each half-bridge submodule is fixed at 20 kHz. The proposed SCF- and SRC-based circulating current controller, average voltage controller, and individual voltage balance controller are implemented on the PLECS RT box, shown in Fig. 21. Parameters of the single-phase MMC and the proposed SCF and SRC-based circulating current controller are given in Tables III and IV, respectively. Fig. 22 shows the multilevel output voltage and output current of a five-level single-phase MMC, which is tested at the 400-V dc

TABLE III
PARAMETERS OF THE SINGLE-PHASE MMC

Parameter name	Symbol	Value
DC link voltage	V_{dc}	400 V
Output AC voltage (rms)	V_o	120 V
Rated power	P_o	1000 W
Number of submodules in each arm	k	2
Submodule capacitor	C	940 μF
Rated capacitor voltage	V_C	200 V
Arm inductance	L_{arm}	2.5 mH
Equivalent arm resistance	R_{arm}	0.1 Ω
PWM strategy		Carrier phase shift PWM
Submodule switching frequency	f_{sm}	20 kHz
MMC equivalent switching frequency	f_{eff}	40 kHz

TABLE IV
CONTROLLER PARAMETERS

Controller	Parameter	Value
Average voltage controller	Proportional Gain & Integral Gain	0.01 & 1
Circulating current controller	Proportional Gain & Integral Gain	0.1 & 1
Repetitive controller	K_{rc}, N_s, N_1	0.03, 20, 1
Spatial Repetitive controller	K_{src}, N_s, N_1	0.03, 20, 1

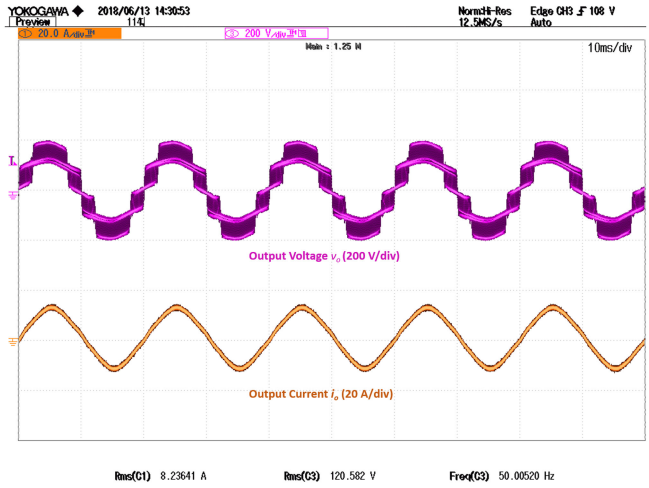

Fig. 22. Experimental results for the output voltage and output current at the 400-V dc input voltage and 1-kW rated power.

input voltage and the 1-kW output power. With the implementation of the average voltage controller and individual voltage balance controller, the upper and lower arm submodule capacitor voltages are maintained equal and are at the reference value of 200 V, shown in Fig. 23.

The performance of the proposed SCF- and SRC-based circulating current control strategy is compared with the traditional cascaded PI-based and notch filter + repetitive-controller-based circulating current controllers. Experimental results for the circulating current reference (which is generated by the outer average voltage control loop), circulating current, and upper and lower arm currents under steady state with the conventional

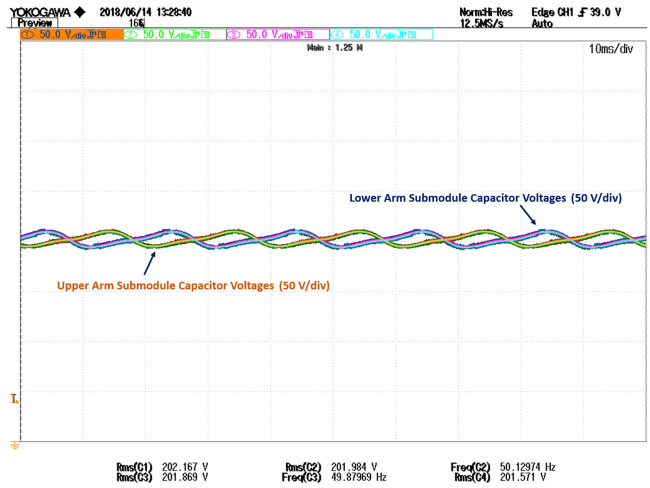

Fig. 23. Experimental results for the upper arm and lower arm submodule capacitor voltages at the 400-V input voltage and 1-kW rated power.

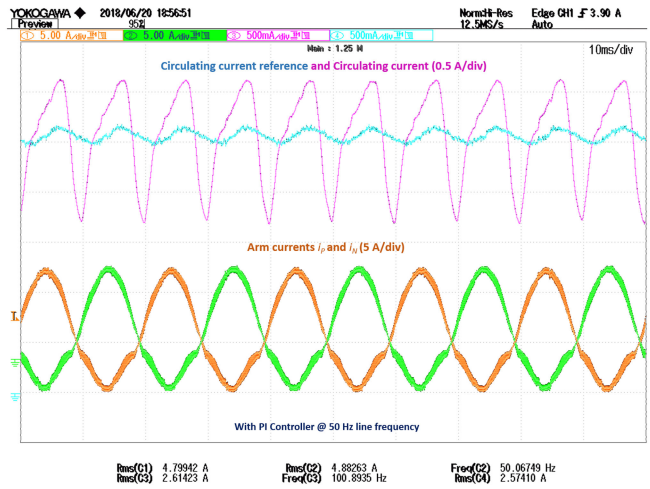

Fig. 24. Experimental results for the circulating current reference, circulating current, and arm currents under steady state with a cascaded PI controller at a rated operating frequency of 50 Hz.

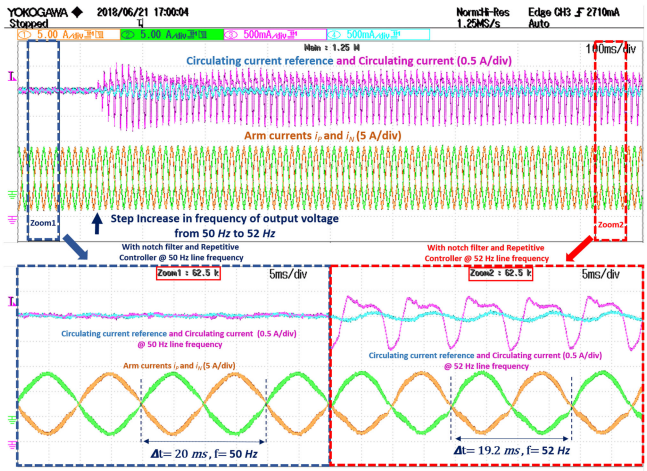

Fig. 25. Experimental results for the circulating current reference, circulating current, and arm currents obtained during a step change in the operating line frequency from 50 to 52 Hz with a notch filter + repetitive controller.

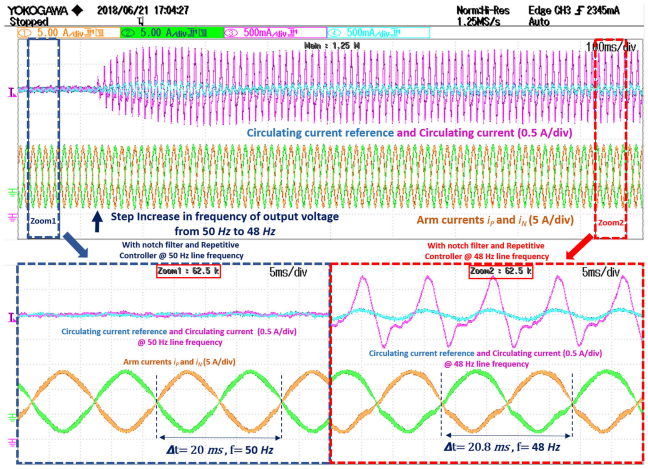

Fig. 26. Experimental results for the circulating current reference, circulating current, and arm currents obtained during a step change in the operating line frequency from 50 to 48 Hz with a notch filter + repetitive controller.

cascaded PI-control-based circulating current controller for a single-phase MMC operating at a 50-Hz line frequency are shown in Fig. 24. We can observe both the circulating current reference (waveform in blue) and actual circulating current (waveform in pink) has unwanted even-order harmonic components in addition to the dc component. The total harmonic distortion (THD) profile of the both the waveforms is given in Fig. 29. As discussed in the earlier sections the 100-Hz component in the circulating current reference is due to the voltage ripple component of v_{csum}, which is fed to the outer total energy control loop. Significant gain of the outer voltage loop PI controller at 100 Hz results in the second-order harmonic in the circulating current reference. We can observe the even-order harmonic components in the actual circulating current are at higher magnitude than in the reference, which is due to harmonics in the arm voltage of the MMC. And also the upper and lower arm currents are non-sinusoidal due to the presence of the dominant second-order harmonic in the circulating current. In addition, the rms value of the circulating current increases due to the presence of even-order harmonics in it. This in-turn increases the power loss in the switching devices of the converter.

Figs. 25 and 26 show the experimental results for the circulating current reference, circulating current, and arm currents obtained during a step change in the operating line frequency with a notch filter + repetitive-controller-based circulating current controller. With the use of the notch filter, tuned to 100 HZ, in the outer total energy control loop and a repetitive controller in addition to the PI controller in the inner circulating current control loop, the second-order harmonic in the circulating current reference and even-order harmonics in the circulating current are alleviated, and hence, the arm currents are sinusoidal, while operating at the rated operating line frequency of 50 Hz. This is due to high attenuation of the notch filter and the high gain offered by the repetitive controller at the specific designed frequency of 100 Hz and at corresponding harmonic frequencies. However, with a change in the operating ac line frequency from 50 to 52 Hz as shown in Fig. 25, or from 50 to 48 Hz as shown in

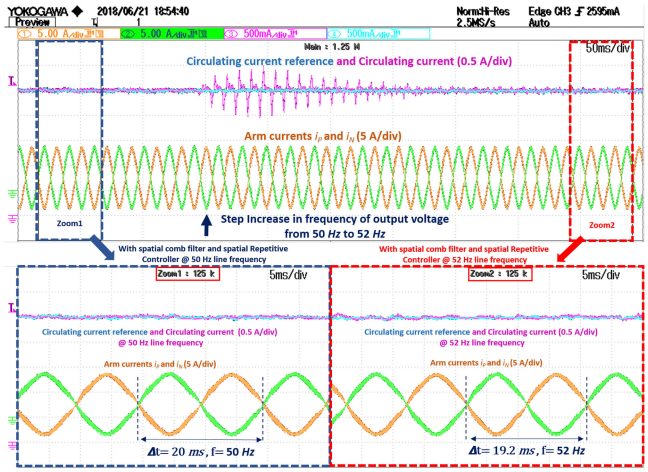

Fig. 27. Experimental results for the circulating current reference, circulating current, and arm currents obtained during a step change in the operating line frequency from 50 to 52 Hz with SCF + SRC.

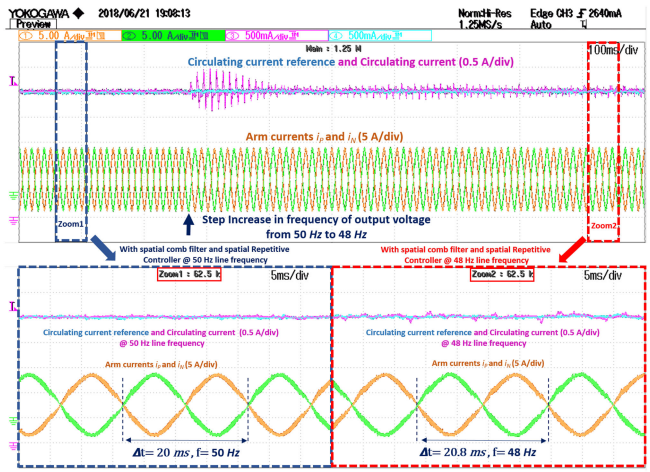

Fig. 28. Experimental results for circulating current reference, circulating current, and arm currents obtained during a step change in operating line frequency from 50 to 48 Hz with SCF + SRC.

Fig. 26, the notch filter + repetitive-controller-based circulating current controller failed to attenuate the even-order harmonics in the both circulating current reference and circulating current. From Fig. 25, one can observe that with the change in the fundamental line frequency to 52 Hz, the dominant second-order harmonic, which is at 104 Hz, and other even-order harmonics have propagated in the circulating current reference and circulating current, and as a result, the arm currents are non-sinusoidal. This is due to variation in the ripple frequency of v_{csum} from 100 to 104 Hz with change in the operating line frequency from 50 to 52 Hz. As per the design, the notch filter offers high attenuation to the 100-Hz component, and the repetitive controller offers high gain to the 100-Hz component and its corresponding harmonic frequencies. Therefore, this control scheme fails to attenuate even-order harmonic components. A similar response is observed when the operating line frequency is changed from 50 to 48 Hz. As shown in Fig. 26, dominant second-order harmonic, which is at 96 Hz, appears in both circulating current reference and circulating current. These even-order harmonics in the circulating current can have an adverse effect on the performance of the MMC.

To substantiate the performance of the proposed control scheme, the same test has been carried out on the 400-V, 1-kW, five-level single-phase MMC with the SCF + SRC-based circulating current controller and the corresponding experimental results for the circulating current reference, circulating current, and arm currents obtained during a step change in the operating line frequency are shown in Figs. 27 and 28. With the use of the SCF, in the outer loop and an SRC in conjunction with the PI controller in the inner loop of the proposed controller, the second-order harmonic in the circulating current reference and even-order harmonics in the circulating current are mitigated and the arm currents became sinusoidal, while operating at the rated operating line frequency of 50 Hz. This is due to high attenuation of the SCF and high gain of the SRC at frequency of 100 Hz and at corresponding harmonic frequencies. Even with a change in the operating ac line frequency from 50 to 52 Hz as shown in Fig. 27, or from 50 to 48 Hz, as shown in Fig. 28, the proposed SCF- and SRC-based circulating current controller efficiently suppresses the even-order harmonics in the both circulating current reference and circulating current,

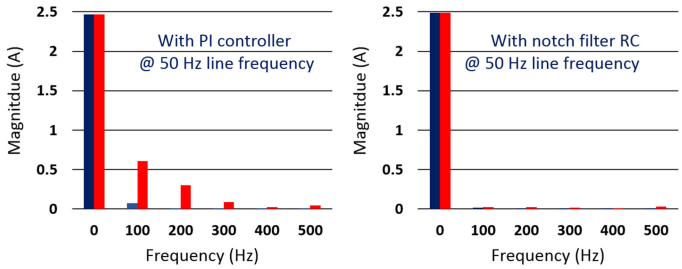

Fig. 29. Comparison of the experimentally obtained THD profile of the circulating current reference (blue) and circulating current (red) with the PI controller and notch filter + repetitive controller at a rated operating frequency of 50 Hz.

thereby, maintaining sinusoidal arm currents. With the change in the operating line frequency from 50 to 52 Hz, the frequency of the second-order harmonic voltage ripple in v_{csum}, which is the driving force for circulating the current harmonics, shifts from 100 to 104 Hz. Even then the proposed controller is able to adaptively tune its gain characteristics to mitigate the propagation of even-order harmonics in the circulating current reference and circulating current, and as a result, the arm currents are maintained sinusoidal, as shown in Fig. 27. A similar performance has been observed when the operating line frequency is changed from 50 to 48 Hz and the controller performance is shown in Fig. 28.

Therefore, from the results presented in Figs. 27 and 28, it is evident that the even-order harmonics in the circulating current reference and circulating current are suppressed by the proposed SCF- and SRC-based circulating current controller even under variation in the operating ac line frequency of the single-phase MMC. A phase sampling circuit is incorporated in the proposed control architecture that enables phase domain sampling. As the phase angle varies always from 0 to 2π, irrespective of the fundamental ac line frequency, by fixing the value of $\Delta\theta$, fixed number of samples can be generated per cycle, thereby, achieving dynamic change in the sampling frequency. This resulted in strong harmonic suppression capability of the proposed SCF- and SRC-based circulating controller irrespective of the variation in the fundamental operating frequency. As the

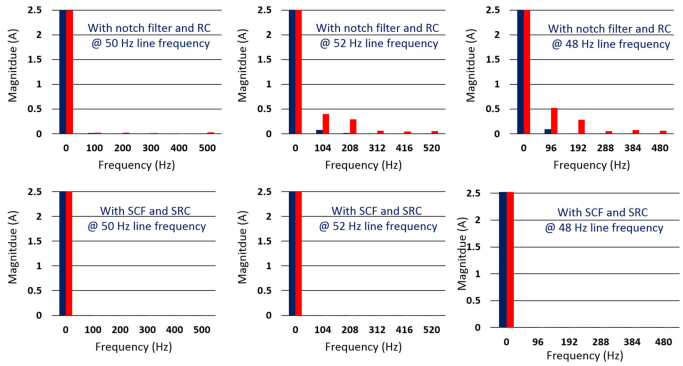

Fig. 30. Comparison of the experimentally obtained THD profile of the circulating current reference (blue) and circulating current (red) with the notch filter + repetitive controller and SCF + SRC at different operating frequencies.

traditional time-domain repetitive controller uses a fixed sampling frequency, the number of samples per cycle is not constant with the change in the operating ac line frequency. Hence, a repetitive-controller-based circulating current controller failed to attenuate the even-order harmonics. The THD performance of the proposed controller is compared with the conventional controller and summarized as shown in Fig. 30. It can be seen that with the proposed controller, even-order harmonics are effectively attenuated in the circulating current even under variable frequency operation of the MMC.

VII. Conclusion

In this paper, a new circulating current control architecture comprising of an SCF and an SRC is proposed to effectively attenuate the even-order harmonics in the circulating current independent of the operating ac line frequency of the MMC. First, a simplified mathematical analysis is presented to dwell into the reason for the presence of the dominant second harmonic in both the circulating current and submodule capacitor voltages. Then, the drawbacks of the existing circulating current control schemes for the MMC are discussed. Afterwards, analysis and design of the proposed circulating current control architecture is presented. Finally, results obtained from a system level simulation model developed on PLECS simulation software and a scaled-down laboratory prototype of a five-level single-phase MMC are presented to demonstrate the performance of the proposed control architecture. Results show that the conventional time-domain-based repetitive controller has failed to attenuate the even-order harmonics in the circulating current, when the operating ac line frequency of the MMC is varied. This is due to the limited harmonic rejection capability of the time-domain-based repetitive controller at variable frequencies. On the other hand, the proposed control architecture with an SCF in the outer loop and an SRC in the inner loop has effectively eliminated the even-order harmonics in both the circulating current reference and the circulating current even under variable frequency operation of the MMC, thereby, improving the steady-state performance.

Acknowledgment

This work has been carried out at the National University of Singapore as a part of the research on "High Voltage AC/DC Power Transmission for Subsea Power System," sponsored by Singapore Maritime Institute in collaboration with Schlumberger Limited, Singapore.

References

[1] M. A. Perez, S. Bernet, J. Rodriguez, S. Kouro, and R. Lizana, "Circuit topologies, modeling, control schemes, and applications of modular multilevel converters," *IEEE Trans. Power Electron.*, vol. 30, no. 1, pp. 4–17, Jan. 2015.

[2] S. Debnath, J. Qin, B. Bahrani, M. Saeedifard, and P. Barbosa, "Operation, control, and applications of the modular multilevel converter: A review," *IEEE Trans. Power Electron.*, vol. 30, no. 1, pp. 37–53, Jan. 2015.

[3] S. Kolluri, N. B. Y. Gorla, R. Sapkota, and S. K. Panda, "A new control approach for improved dynamic performance of MMC based HVDC subsea power transmission system," in *IEEE Innov. Smart Grid Technol.—Asia*, Dec. 2017, pp. 1–6.

[4] R. Sapkota, S. Kolluri, J. Adhikari, and S. K. Panda, "Fault identification algorithm for MMC based hybrid high voltage dc transmission system for deep-water oil and gas processing," in *Proc. 19th Eur. Conf. Power Electron. Appl.*, Sep. 2017, pp. P.1–P.8.

[5] R. Sapkota, S. Kolluri, J. Adhikari, and S. K. Panda, "MMMC based multiterminal HVDC subsea power transmission system with the integration of offshore renewable energy," in *Proc. IEEE Innov. Smart Grid Technol.—Asia*, Dec. 2017, pp. 1–6.

[6] M. Malinowski, K. Gopakumar, J. Rodriguez, and M. A. Perez, "A survey on cascaded multilevel inverters," *IEEE Trans. Ind. Electron.*, vol. 57, no. 7, pp. 2197–2206, Jul. 2010.

[7] A. Lesnicar and R. Marquardt, "An innovative modular multilevel converter topology suitable for a wide power range," in *Proc. IEEE Bologna Power Tech Conf.*, Jun. 2003, vol. 3, pp. 1–6.

[8] M. Glinka and R. Marquardt, "A new ac/ac multilevel converter family," *IEEE Trans. Ind. Electron.*, vol. 52, no. 3, pp. 662–669, Jun. 2005.

[9] S. Allebrod, R. Hamerski, and R. Marquardt, "New transformerless, scalable modular multilevel converters for HVDC-transmission," in *Proc. IEEE Power Electron. Spec. Conf.*, Jun. 2008, pp. 174–179.

[10] X. Li, Q. Song, W. Liu, S. Xu, Z. Zhu, and X. Li, "Performance analysis and optimization of circulating current control for modular multilevel converter," *IEEE Trans. Ind. Electron.*, vol. 63, no. 2, pp. 716–727, Feb. 2016.

[11] M. Vasiladiotis, N. Cherix, and A. Rufer, "Accurate capacitor voltage ripple estimation and current control considerations for grid-connected modular multilevel converters," *IEEE Trans. Power Electron.*, vol. 29, no. 9, pp. 4568–4579, Sep. 2014.

[12] G. Konstantinou, J. Pou, S. Ceballos, R. Picas, J. Zaragoza, and V. G. Agelidis, "Utilising redundant voltage levels for circulating current control in modular multilevel converters," in *Proc. 41st Annu. Conf. Ind. Electron. Soc.*, Nov. 2015, pp. 002213–002218.

[13] G. Bergna *et al.*, "An energy-based controller for HVDC modular multilevel converter in decoupled double synchronous reference frame for voltage oscillation reduction," *IEEE Trans. Ind. Electron.*, vol. 60, no. 6, pp. 2360–2371, Jun. 2013.

[14] M. A. Prez, R. L. F., and J. Rodriguez, "Decoupled current control of modular multilevel converter for HVDC applications," in *Proc. IEEE Int. Symp. Ind. Electron.*, May 2012, pp. 1979–1984.

[15] X. She, A. Huang, X. Ni, and R. Burgos, "AC circulating currents suppression in modular multilevel converter," in *Proc. 38th Annu. Conf. IEEE Ind. Electron. Soc.*, Oct. 2012, pp. 191–196.

[16] M. Zhang, L. Huang, W. Yao, and Z. Lu, "Circulating harmonic current elimination of a CPS-PWM-based modular multilevel converter with a plug-in repetitive controller," *IEEE Trans. Power Electron.*, vol. 29, pp. 2083–2097, Apr. 2014.

[17] L. He, K. Zhang, J. Xiong, and S. Fan, "A repetitive control scheme for harmonic suppression of circulating current in modular multilevel converters," *IEEE Trans. Power Electron.*, vol. 30, no. 1, pp. 471–481, Jan. 2015.

[18] S. Yang, P. Wang, Y. Tang, M. Zagrodnik, X. Hu, and K. J. Tseng, "Circulating current suppression in modular multilevel converters with even-harmonic repetitive control," *IEEE Trans. Ind. Appl.*, vol. 54, no. 1, pp. 298–309, Jan. 2018.

[19] S. D'Arco, A. Petterteig, R. Pittini, and T. M. Undeland, "Droop regulated VSCs for island operation of future offshore systems," in *Proc. IEEE Trondheim PowerTech*, Jun. 2011, pp. 1–6.

[20] B. Bahrani, S. Debnath, and M. Saeedifard, "Circulating current suppression of the modular multilevel converter in a double-frequency rotating reference frame," *IEEE Trans. Power Electron.*, vol. 31, no. 1, pp. 783–792, Jan. 2016.
[21] Q. Tu, Z. Xu, and J. Zhang, "Circulating current suppressing controller in modular multilevel converter," in *Proc. 36th Annu. Conf. IEEE Ind. Electron. Soc.*, Nov. 2010, pp. 3198–3202.
[22] S. Li, X. Wang, Z. Yao, T. Li, and Z. Peng, "Circulating current suppressing strategy for MMC-HVDC based on nonideal proportional resonant controllers under unbalanced grid conditions," *IEEE Trans. Power Electron.*, vol. 30, no. 1, pp. 387–397, Jan. 2015.
[23] S. Dasgupta, S. K. Sahoo, S. K. Panda, and G. A. J. Amaratunga, "Single-phase inverter-control techniques for interfacing renewable energy sources with microgrid—Part II: Series-connected inverter topology to mitigate voltage-related problems along with active power flow control," *IEEE Trans. Power Electron.*, vol. 26, no. 3, pp. 732–746, Mar. 2011.
[24] S. Kolluri, P. Thummala, R. Sapkota, J. X. Xu, and S. K. Panda, "Spatial repetitive controller for minimizing circulating harmonic currents in modular multilevel converters for variable frequency applications," in *Proc. 42nd Annu. Conf. IEEE Ind. Electron. Soc.*, Oct. 2016, pp. 3612–3617.
[25] S. Dasgupta, S. K. Sahoo, and S. K. Panda, "Single-phase inverter control techniques for interfacing renewable energy sources with microgrid—Part I: Parallel-connected inverter topology with active and reactive power flow control along with grid current shaping," *IEEE Trans. Power Electron.*, vol. 26, no. 3, pp. 717–731, Mar. 2011.
[26] M. Hagiwara and H. Akagi, "Control and experiment of pulsewidth-modulated modular multilevel converters," *IEEE Trans. Power Electron.*, vol. 24, no. 7, pp. 1737–1746, Jul. 2009.
[27] S. Kolluri, N. B. Y. Gorla, R. Sapkota, and S. K. Panda, "A repetitive and Lyapunov function-based control approach for improved steady state and dynamic performance of modular multilevel converters," in *Proc. 43rd Annu. Conf. IEEE Ind. Electron. Soc.*, Oct. 2017, pp. 687–692.
[28] S. Kolluri, N. B. Y. Gorla, R. Sapkota, and S. K. Panda, "Spatial repetitive controller for improved steady state performance of droop regulated modular multilevel converter in wind farm application," in *Proc. IEEE Appl. Power Electron. Conf. Expo.*, Mar. 2018, pp. 1673–1678.
[29] P. Mattavelli, L. Tubiana, and M. Zigliotto, "Torque-ripple reduction in PM synchronous motor drives using repetitive current control," *IEEE Trans. Power Electron.*, vol. 20, no. 6, pp. 1423–1431, Nov. 2005.
[30] J. Lyu, X. Cai, and M. Molinas, "Frequency domain stability analysis of MMC-based HVDC for wind farm integration," *IEEE J. Emerg. Sel. Topics Power Electron.*, vol. 4, no. 1, pp. 141–151, Mar. 2016.

Sandeep Kolluri (S'16) received the B.Tech. degree in electrical and electronics engineering from the Acharya Nagarjuna University, Guntur, India, in 2011, and the M.S. (by research) degree in power electronics from the Indian Institute of Technology Madras, Chennai, India, in 2014. He is currently working toward the Ph.D. degree in electrical engineering with the National University of Singapore, Singapore.

He was with the Department of Electrical and Computer Engineering, National University of Singapore, from July 2014 to July 2015, as a Research Engineer. His research interests include modular multi-level converters, dc–dc converters, and control of power electronic converters for energy management in hybrid electric vehicles.

Naga Brahmendra Yadav Gorla (S'15) received the M.S. degree (by research) from the Indian Institute of Technology Madras, Chennai, India, in 2013. Since January 2015, he has been working toward the Ph.D. degree with the Electrical Machines and Drives Lab, National University of Singapore, Singapore.

He was with the Electrical and Electronics Department, Singapore Polytechnic, as a Research Engineer between October 2013 and December 2015. His research interests include power quality improvement in grid-connected inverters and rectifiers, fault detection and localization in multilevel converters, fault tolerance and resiliency in multilevel converters, and solid-state transformer architectures and control.

Rajesh Sapkota received the Bachelor of Technology degree in electrical engineering from National Institute of Technology, Kurukshetra, India, in 2011, and the Master of Science degree in power engineering from Nanyang Technological University, Singapore, in 2015.

He is currently working as a Research Engineer with the Department of Electrical and Computer Engineering, National University of Singapore, Singapore. He has previously worked with Schneider Electric, Mumbai, India, as a Field Service Engineer in the field of retrofitting and revamping of LV/MV switchgears. His research interests include modeling of subsea cable, voltage source converters, modeling, control, and operation of the modular-multilevel-converter-based HVdc grid for the power supply to distant oil and gas facilities and offshore renewable energy integration, and fault identification protection of the HVdc grid.

Sanjib Kumar Panda (S'86–M'91–SM'01) received the B.Eng. degree from the South Gujarat University, Surat, India, in 1983, the M.Tech. degree from the Indian Institute of Technology, Banaras Hindu University, Varanasi, India, in 1987, and the Ph.D. degree from the University of Cambridge, Cambridge, U.K., in 1991, all in electrical engineering.

Since 1992, he has been holding a Faculty Position with the Department of Electrical and Computer Engineering, National University of Singapore, Singapore, and currently serving as an Associate Professor and the Director of the Power & Energy Research Area. He has authored and coauthored more than 200 peer reviewed research papers, coauthored one book, and contributed to several book chapters and six patents. His research interests include high-performance control of motor drives and power electronic converters, condition monitoring and condition-based maintenance, building energy efficiency, etc.

Dr. Panda received the Cambridge-Nehru Scholarship and M. T. Mayer Graduate Scholarship during his Ph.D. study (1987–1991). He is serving as an Associate Editor of several IEEE Transactions and the Editor of the *Journal of Power Electronics*, South Korea. He has served in various capacities for the two key conferences: the IEEE Power Electronics and Drive Systems Conference and the IEEE International Conference on Sustainable Energy Technologies Conference series organized and managed by the IEEE Joint Industry Applications Society/ Power Electronics Society (PELS) Society Chapter, Singapore Section. He has served the IEEE Section Congress 2014 as a Member of the Program Committee. He is serving as the IEEE R-10 Asia Pacific Liaison Officer for the IEEE PELS. He was the recipient of the IEEE Third Millennium Medal, the IEEE Singapore Section Outstanding Volunteer Award in 2010, and the IEEE Region-10 Outstanding Volunteer Award in 2014.